INTERNATIONAL SOCIETY FOR
SOIL MECHANICS AND
GEOTECHNICAL ENGINEERING

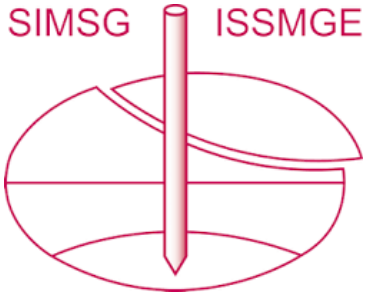

This paper was downloaded from the Online Library of the International Society for Soil Mechanics and Geotechnical Engineering (ISSMGE). The library is available here:

https://www.issmge.org/publications/online-library

This is an open-access database that archives thousands of papers published under the Auspices of the ISSMGE and maintained by the Innovation and Development Committee of ISSMGE.

The paper was published in the proceedings of the 20th International Conference on Soil Mechanics and Geotechnical Engineering and was edited by Mizanur Rahman and Mark Jaksa. The conference was held from May 1st to May 5th 2022 in Sydney, Australia.

Proceedings of the 20th International Conference on Soil Mechanics and Geotechnical Engineering– Rahman and Jaksa (Eds)
© 2022 Australian Geomechanics Society, Sydney, Australia, ISBN 978-0-9946261-4-1

Quantification of the geogrid-aggregate stiffened zone using bender element field sensors

Quantification de la rigidification de la zone géogrille-agrégat à l'aide d'éléments piézoélectriques de type BE

Erol Tutumluer, Mingu Kang, Issam I.A. Qamhia & Han Wang
Department of Civil and Environmental Engineering, University of Illinois at Urbana-Champaign, USA
tutumlue@illinois.edu

Jeb S. Tingle
Engineer Research and Development Center, US Army Corps of Engineers, USA

ABSTRACT: This paper focuses on the evaluation of the stiffened zone in a geogrid-stabilized unbound aggregate pavement base using the newly developed bender element (BE) field sensors. A bender element pair can be used as a system of shear wave transducers to evaluate the local stiffness increase of a conventional asphalt pavement base layer in the vicinity of installed geogrids. Such an unbound aggregate base layer has been recently constructed in large-scale laboratory box tests and installed with a triangular aperture geogrid to evaluate the geogrid stiffened zone at the University of Illinois. With shear wave velocities measured at three different heights using three BE pairs, vertical stiffness profiles of the mechanically stabilized aggregate were successfully evaluated above the geogrid. In addition, dynamic cone penetration (DCP) and Light Weight Deflectometer (LWD) tests were performed on the surface of the unbound aggregates. The stiffness increases evaluated owing to the geogrid enhancement and extent of the local stiffened zone were compared to those quantified from geogrid-stabilized laboratory triaxial test specimens.

RÉSUMÉ : Cet article se concentre sur l'évaluation de la zone rigidifiée d'une base stabilisée par géogrille à l'aide d'éléments piézoélectriques de type BE nouvellement développés. Une paire d'élément piézoélectriques peut être utilisée comme système de transducteurs d'ondes en cisaillement pour évaluer l'augmentation de la rigidité locale à proximité de géogrilles installées dans une base de chaussée typique en enrobé bitumineux. Une telle structure de chaussée a été récemment construite en laboratoire à l'Université de l'Illinois avec une boite géotechnique incorporant une géogrille à ouverture triangulaire pour évaluer la zone rigidifiée. La vitesses d'onde en cisaillement a été mesurée à trois endroits différents, à l'aide de trois paires d'éléments de type BE. Le profil de rigidité de la base au-dessus de la géogrille a été évalué avec succès. De plus, un essai au pénétromètre à cône dynamique (DCP) et au déflectomètre léger à masse tombante (LWD) ont été réalisés sur la surface de la base. L'augmentation de rigidité attribuée à la géogrille et l'étendue de la zone locale rigidifiée ont été évaluées à partir des résultats mesurés en laboratoire.

KEYWORDS: Geogrid, aggregate stiffness, bender element field sensor, shear wave velocity, mechanical stabilization.

1 INTRODUCTION

Geogrids used for stabilization in asphalt surfaced pavements are beneficial to increase confinement by immobilizing unbound aggregates, increase bearing capacity of the layered system, prevent excessive rutting under vehicular loading, and eventually extend the pavement service life. Geogrids typically installed in a pavement unbound aggregate base or subbase provide the essential mechanism of lateral restraint and create a stiffened zone in the proximity of the geogrid location. Numerous experimental research studies reported that using geogrids to stabilize unbound layers effectively reduced the amount of pavement surface deformation (Barker, 1987; Webster, 1993; Tingle & Jersey, 2009; Chen et al., 2018; Norwood, 2019). To examine the stiffening effect through the geogrid-aggregate interlocking, Kwon and Tutumluer (2009) conducted dynamic cone penetrometer (DCP) testing. The DCP test results showed a stiffer layer was formed near geogrid due to interlocking between geogrid and aggregates. Another experimental approach involves utilizing a pullout test to study the load transfer mechanism and the pullout strength of a geogrid (Sugimoto & Alagiyawanna, 2003; Moraci & Recalcaati, 2006; Peng and Zornberg, 2017). Furthermore, experimental approaches which use falling weight deflectometer (FWD) and lightweight deflectometer (LWD) tests have been studied by several researchers, although the results often varied and somewhat inconsistent findings were reported depending on the experimental conditions (Kinney et al., 1998; Tingle & Jersey, 2009; Tang et al, 2013). Numerical studies using the Discrete Element Method (DEM) or Finite Element Method (FEM) have also been conducted to assess the effect of geogrid stabilization in pavement unbound aggregate layers, and the simulation results revealed the existence of a stiffened zone in the vicinity of geogrids (Konietzky et al., 2004; McDowell et al., 2006; Tutumluer et al., 2009; Zhou et al., 2012; Chen et al., 2014; Qian et al., 2015). While various research approaches have been undertaken to evaluate such a geogrid-stiffened zone near geogrid, direct quantification of the modulus increase or stiffening effect and the extend of such a stiffened zone was unavailable in past studies.

One of the widely used experimental approaches to demonstrate the benefit of using geogrid involves building test sections with geogrids, in the field or laboratory, to evaluate the effect of geogrid stabilization on pavement deformation under static or dynamic loading. To directly measure and quantify the amount of local stiffening and the extent of the stiffened zone in the test section, a recent approach taken at the University of Illinois has utilized shear wave transducers in the influence zone near geogrid. Shear wave transducers, e.g. bender elements (BEs), have been commonly used to evaluate the stiffness characteristics of granular materials in laboratory studies (Lee et al, 2005). Recent studies using bender element pairs to measure the shear wave velocity of geogrid-stabilized aggregate specimens during soil triaxial testing confirmed that specially designed BE pairs were capable of evaluating the characteristics

of geogrid-stiffened zone, i.e. changes in shear wave velocity along with depth above the geogrid (Byun & Tutumluer, 2017; Kang et al., 2020). Furthermore, Kang et al. (2021) developed a bender element (BE) field sensor to monitor and evaluate the shear wave velocity changes of geogrid stabilized and non-stabilized aggregate base layers of in-situ constructed pavements or full-scale pavement test sections.

The objective of this paper is to quantify the stiffening effect and the extent of the stiffening zone owing to the geogrid stabilization for the aggregate layer using a large-scale laboratory testbed. A bender element (BE) field sensor is utilized to evaluate the local stiffness of unbound aggregates in the proximity of geogrids through shear wave velocity measurements. In addition, DCP and LWD tests were also conducted on the surface of the test specimens. Dense-graded crushed stone aggregates were placed in a large-scale laboratory testbed over a geofoam layer. Experiments were performed with five levels of static surcharge loadings which provided different confinement levels. The geogrid was installed near the bottom of the aggregate layer for the mechanically stabilized aggregate layer, whereas the control sections were compacted without geogrid. Two punched and drawn geogrids with different sizes of triangular aperture were evaluated. Shear wave velocities were measured using a BE field sensor installed at three different heights above the geogrid. Finally, shear wave velocities and stiffness properties measured under different testing arrangements were investigated.

2 EXPERIMENTAL SETUP

2.1 *Shear wave measurement system*

In this study, a recently developed BE field sensor was utilized to measure the shear wave velocity of constructed aggregate layers. The BE field sensor was developed for the estimation of the in-situ stiffness of the pavement base and subbase layer through the shear wave velocity measurement (Kang et al., 2021). The BE field sensor consists of a pair of BE transducers, BE transducer protection module and a metal frame that maintains a fixed distance between the pair of BE transducers and protects the cable. A schematic drawing of the BE field sensor used in this study is shown in Figure 1. The BE transducer is composed of a thin metal plate sandwiched between two piezoceramic plates. The piezoceramic plates vibrate when an electrical charge applied, and the physical deformation of the piezoceramic plate generates the electrical charge conversely. Thus, a BE can be utilized as either an elastic wave source or receiver. BE sensors have been widely used in laboratory testing owing to the great coupling ability between the transducer and granular materials such as soil and aggregates (Lee et al., 2005).

Figure 1 shows a schematic drawing of the BE field sensor measurement system for the measurement of the shear wave velocity. The system consists of a signal generator, a linear amplifier, an oscilloscope, a filter-amplifier and a computer. A signal generator generates and delivers a sinusoidal wave to the linear amplifier and oscilloscope. A linear amplifier amplifies a signal up to 6 times to deliver enough energy to the source BE transducer. The receiver BE transducer collects the elastic wave propagating through the specimen and then delivers an electrical signal to the filter-amplifier. After the signal conditioning using the filter-amplifier, and the output signal is collected by the oscilloscope. A signal averaging using an oscilloscope with a stacking number of 1,024 increases the strength of the signal. To collect a clear output signal with a high signal-to-noise ratio, the frequency of the input sinusoidal wave applied is usually the resonant frequency of the specimens (Clayton, 2011).

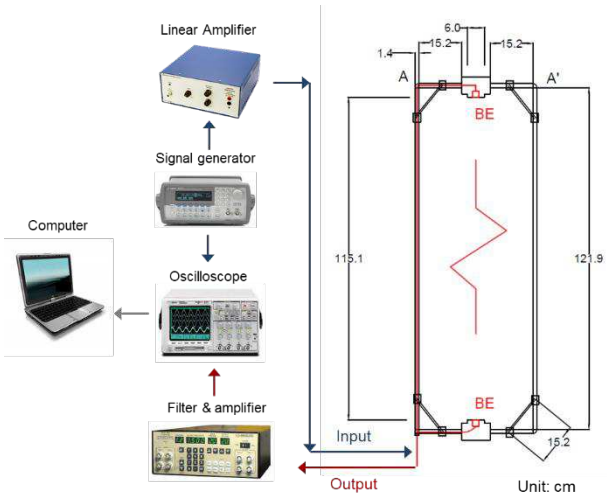

Figure 1. Shear wave measurement system configuration with Bender Element field sensor.

2.2 *Test setup*

To perform the experiment for the geogrid performance evaluation, a large-scale calibration testbed was constructed. The dimension of the testbed was 182.9 cm (6 ft.) by 182.9 cm (6 ft.) by 61.0 cm (2 ft.) (length by width by height) to provide sufficient space to build base and subbase layers with multiple layers of sensors. Expanded polystyrene (EPS) geofoams have commonly been used in laboratory tests as a uniform subgrade owing to the target low strength properties (Zou et al., 2000; Siabil et al., 2020). In this study, a 15.2 cm (6-in.) thick expanded polystyrene (EPS) geofoam was installed at the bottom of the testbed as a soft subgrade. From multiple California Bearing Ratio (CBR) tests conducted, the CBR of the geofoam was determined to be 5%, which corresponds to a low strength for a soft fine-grained subgrade (Yoder & Witczak, 1991; NCHRP 1-37A, 2004). A 45.8-cm (18-in.) thick base course aggregate layer was constructed in the testbed above the geofoam. To maintain consistent test conditions for each test, oven-dry aggregates were used. The aggregate material was compacted in four lifts using a vibratory plate compactor maintaining a consistent number of compactor passes for each lift to achieve a uniform compaction effort. The achieved dry densities of the aggregate lifts were typically around 18.61 kN/m^3 (118.5 pcf), much lower than the MDD value of 22.2 kN/m^3 (141.4 pcf) owing to the dry condition.

Table 1 lists the sensor location and the distance from the geogrid for each test section constructed in this study. For the geogrid-stabilized sections (tests 1, 2, 4 and 6), the two triangular aperture geogrids used are referred to herein as GG1 and GG2. The GG1 (geogrid having a larger size of aperture) and GG2 were both placed at the bottom location one at a time to investigate the effect of geogrid aperture size conducted in test 1 with one BE field sensor. The GG2 was also placed at 10.2 cm (4-in.) above the bottom of the base layer. BE field sensors were installed in the base layer at three different heights based on the testing scenario. For comparison, shear wave measurement tests were also performed with the BE field sensor placed at the same three locations without any geogrid reinforcement (tests 3, 5 and 7). A schematic drawing of the laboratory testbed with geogrid and BE field sensor is shown in Figure 2.

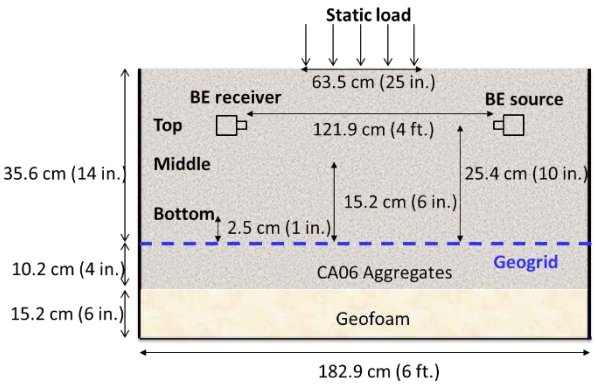

Figure 2. Schematic drawing of the test setup.

Table 1. Summary of the sensor locations and the test setups.

Test no.	Sensor location	Distance from geogrid (cm)	Geogrid placement
1	Bottom	2.5	GG1
2	Bottom	2.5	GG2
3	Bottom	2.5	No Geogrid
4	Middle	15.2	GG2
5	Middle	15.2	No Geogrid
6	Top	25.4	GG2
7	Top	25.4	No Geogrid

2.3 *Aggregate and geogrid properties*

A crushed dolomite material from a local quarry in Illinois was used in the experiments. The grain size distribution determined by dry sieving according to ASTM C136 testing method is shown in Figure 3. The dashed lines indicate the CA06 dense-graded aggregate base course gradation band of the Illinois Department of Transportation (IDOT) specification, and the aggregates used for the experiment is in accordance with the specification. The aggregate material is classified as SP-SM (poorly graded sand with silt) according to the Unified Soil Classification System (USCS), and as A-1-a (stone fragments, gravel, and sand) according to AASHTO soil classification. The Nominal Maximum Aggregate Size (NMAS) is 12.5 mm (0.49 in.), and the percent of passing No. 200 sieve size (0.075-mm opening) is 6%. The average particle size (D_{50}) corresponding to a sieve size which 50% of the material passes is 3.08-mm (0.12-in.) in the gradation chart.

Table 2 summarizes detailed information on the aggregate properties including particle size distribution, coefficient of uniformity (Cu), coefficient of curvature (Cc), and gravel to sand ratio (ratio of gravel-sized material retained on No. 4 sieve to sand-size materials passing No. 4 sieve but retained on No. 200 sieve as per USCS). The Maximum Dry Density (MDD) determined by modified Proctor (ASTM D1557) tests is 22.2 kN/m^3 (141.4 pcf) at an optimum moisture content of 6.5% for this material. To maintain consistent test conditions for each test, oven-dry aggregates were used.

Table 3 lists the properties of the two punched and drawn geogrids (GG1 and GG2) with triangular-shaped apertures but different aperture sizes geogrids that were used in the experiments. Note that the effectiveness of the mechanical stabilization using geogrid is affected by geogrid aperture shape and size (Jewell et al., 1984).

Table 2. Properties of the dense-graded crushed aggregate material.

D_{10} (mm)	D_{30} (mm)	D_{50} (mm)	D_{60} (mm)	Cu	Cc	Gravel to Sand (G/S) ratio
0.15	1.53	3.08	4.38	28.36	3.46	0.66

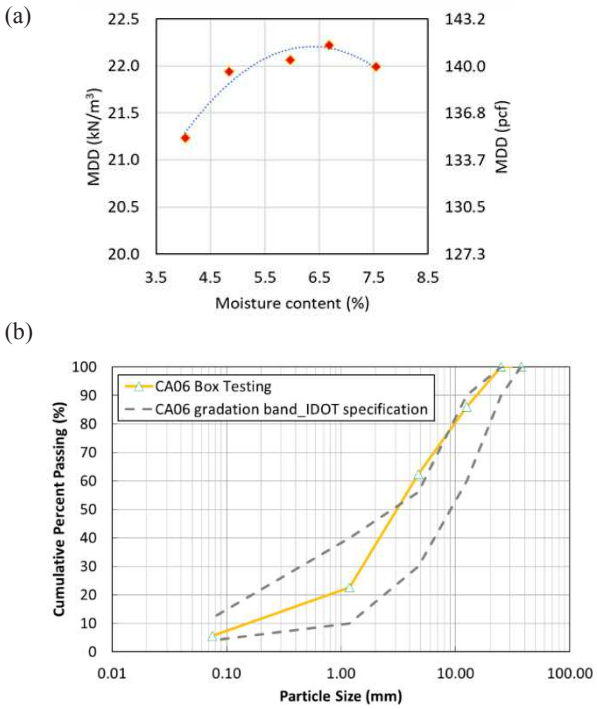

Figure 3. Material properties for the dense-graded aggregate: (a) moisture-density relationship, and (b) grain size distribution in comparison to IDOT's CA06 dense-graded aggregate gradation band.

Table 3. Properties of GG1 and GG2 geogrids.

Index property	Geogrid #1 (GG1)			Geogrid #2 (GG2)		
	Long.	Diag.	Trans.	Long.	Diag.	Trans.
Rib pitch (mm)	40	40		33	33	
Mid-rib depth (mm)		1.3	1.2		1.6	1.2
Mid-rib width (mm)		0.9	1.2		0.4	0.7
Diameter of largest inscribed circle, (mm)		23.1			19.1	

2.4 *Test Procedure*

To quantify the effect of geogrid stabilization on local stiffness increase near geogrid due to aggregate-geogrid interlocking, shear wave signals were collected at three different heights above the geogrid location, referred to herein by top, middle and bottom (see Figure 2). Shear waves were collected with five different levels of static surcharge loads applied on the surface of the unbound aggregate layer. Static surcharge loads were applied on a rigid rectangular loading plate with dimensions 63.5 cm (25 in.) by 53.3 cm (21 in.). Static loadings were applied incrementally, and shear wave velocities were measured at five loading levels. Note that the maximum applied static load was 2.85 kN, which

is equivalent to the wheel load of a sub-compact car (EPA, 2020). Table 4 lists the loading sequence and magnitudes.

Table 4. Loading sequence for the static loading and unloading tests.

Load no.	Static load, kN (lb.)	Static vertical stress, kPa (psi)
1	0.00 (0)	0.00 (0.00)
2	0.67 (151)	1.97 (0.29)
3	1.32 (297)	3.89 (0.56)
4	1.94 (436)	5.72 (0.83)
5	2.85 (641)	8.41 (1.22)

3 TEST RESULTS AND DISCUSSION

3.1 *Shear wave velocity measurements*

The shear wave velocities measured at five stages of static loading are presented in Figure 4. The shear wave velocity was calculated from the distance between the source BE transducer tip and the receiver BE transducer tip and the first arrival time of the signal as follows:

$$V_S = \frac{L}{t_{tip-tip}} \quad (1)$$

where $t_{tip-tip}$ is the first arrival time of the shear wave, and L is the distance between the two BE transducers. Shear wave velocity is a function of stiffness of the specimen, which can be expressed by the following equation (Santamarina et al., 2001):

$$V_S = \left(\frac{G_{max}}{\rho}\right)^{0.5} = \left(\frac{a\sigma_c{}^b}{\rho}\right)^{0.5} \quad (2)$$

where ρ is density of the specimen, G_{max} is a small strain shear modulus, a and b are model parameters determined from regression analysis, and σ_c is the confining pressure applied on the specimen.

Shear wave velocities with geogrid stabilization using GG2 are represented by the solid lines, and shear wave velocity without stabilization is shown with dashed lines. In addition, shear wave velocities with geogrid stabilization using GG1 are shown as only symbols. Note that the tests with GG1 were only performed at the bottom location. Shear wave velocity is primarily influenced by confining stress. Hence, the shear wave velocity for each test gradually increased with the higher magnitude of vertical stress, although the changes of the elastic moduli with vertical stress were small owing to the low magnitudes of applied vertical stresses. Similarly, shear wave velocity gradually increases with the increasing depth due to the confinement from the gravitational load of the upper layer. A comparison between the shear wave velocities with geogrid stabilization and without stabilization clearly shows the geogrid-stiffening effect. The shear wave velocities measured from the BE sensors at the middle and the bottom location with GG2 (tests 1, 2 and 4) were higher than the velocities from the BE sensors without stabilization (tests 3 and 5), whereas the shear wave velocities of stabilized and unstabilized sections were in a similar range at the top location (tests 6 and 7). At load stage 5, geogrid stabilization with GG2 resulted in 7.9% and 6.4% higher shear wave velocities at the bottom and middle locations, respectively. A rapid increase in shear wave velocity from the top to the middle location indicates the range of the stiffened zone. On the other hand, there was no geogrid-stiffening effect at the top location. Thus, it can be concluded that the stiffened zone generated by geogrid stabilization extends more than 15.2 cm (6 in.) above the geogrid location, but the geogrid effect completely diminished at a height of 25.4 cm (10 in.) above the geogrid. In terms of geogrid aperture size, the extent of the geogrid stiffened zone ranged from 8 to 13.3 times the geogrid aperture size.

The shear wave velocities measured from the BE sensors at the bottom location with GG1 and GG2 (tests 1 and 2) indicate that GG2 stabilization provides stiffness enhancement more effectively. At the load stage 5, the shear wave velocity measured at the bottom location increased by 7.9% with GG2 stabilization compared to unstabilized section, whereas the velocity only increased by 4.2% with GG1 stabilization. In a previous study, Kang et al. (2020) estimated local stiffness enhancements with GG1-and GG2-stabilized aggregates from repeated load triaxial testing and concluded that GG2 stabilization led to better geogrid-aggregate interlocking than GG1 which is in accordance with the current test results. However, the amount of shear wave velocity increase was significantly lower than the previous study results, which reported increases in shear wave velocity up to 250%. The difference in the stiffening effect can be attributed to two factors. To start with, the applied confining pressures and the compaction densities achieved in this study were remarkably lower than those of the previous study (~84% of the MDD achieved in aggregate lift construction in the testbed). In addition, in this study, a gravel to sand (G/S) ratio of only 0.66 was reported for the aggregate material tested while the triaxial specimen G/S ratio in the previous study was close to 1.5, which was suggested by Xiao et al. (2012) for the densest aggregate packing. The insufficiency in enhancement compared with previous study may lead to the low shear wave velocity increase.

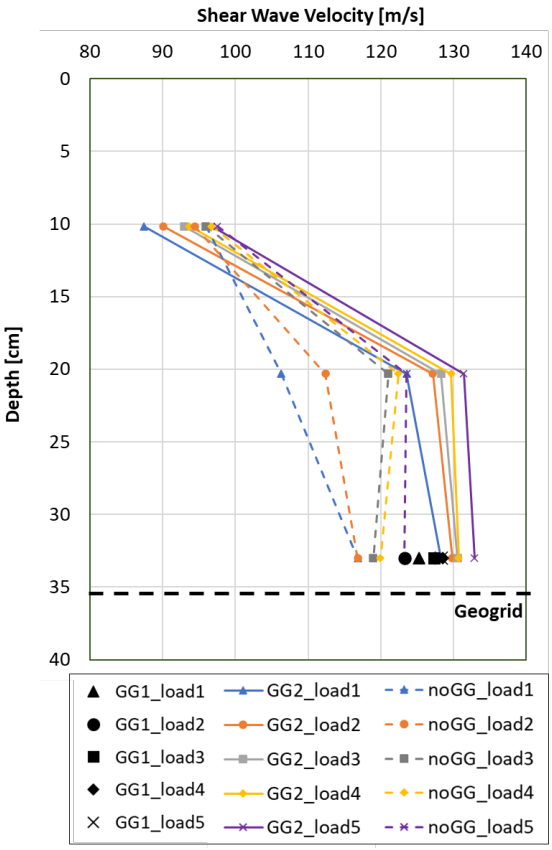

Figure 4. Shear wave velocities measured at five stages of static loading for GG1- and GG2-stabilized sections and non-stabilized sections.

3.2 *Dynamic cone penetrometer (DCP) test results*

After the shear wave velocity measurement for each test section, dynamic cone penetrometer (DCP) tests were performed on the unbound aggregates at the center of the testbed as per ASTM D6951 test method. Figure 5 shows the number of DCP blows needed to penetrate through the unbound aggregate base in the testbed from the surface to the geogrid location for tests 1, 2 and 3 (see Table 1). Higher numbers of blows required in the geogrid-stabilized test section indicate that higher stiffnesses were achieved in the unbound aggregates of the geogrid-stabilized sections (Kwon & Tutumluer, 2009). The number of DCP blows to reach the geogrid location was 29, 26, and 23 for the GG2-stabilized section, GG1-stabilized section, and non-stabilized section, respectively. The higher number of blow count in the GG2-stabilized section than that in the GG1-stabilized section indicates that the GG2-stabilization was more effective in enhancing aggregate stiffness, which is in accordance with the BE field sensor test results by Kang et al. (2020). The range between the orange dashed lines in Figure 5 represents the potential upper bound of the geogrid-stiffened zone concluded from the BE field sensor tests. It is notable that the slope of the accumulated blow count for the GG2-stabilized section increased in the range of the geogrid-stiffened zone.

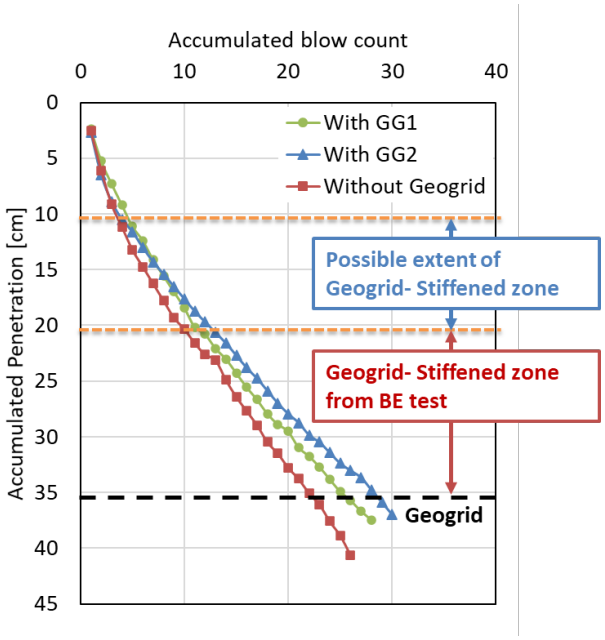

Figure 5. Accumulated DCP blow counts for GG1- and GG2-stabilized sections and non-stabilized sections (Test 1, 2 and 3).

3.3 *Lightweight deflectometer (LWD) test results*

Light Weight Deflectometer (LWD) tests were conducted on the surface of the unbound aggregates after the shear wave velocity measurement for each test section at five different locations according to ASTM E2835 test method. A portable LWD (ZORN ZFG 3.0) which has a 300-mm diameter loading plate was utilized in this study. In addition to the center of the testbed, four test locations selected were 61 cm (2 ft) apart from the center of the testbed to north, south, west, and east, respectively. Table 5 summarizes the average values of the surface resilient moduli measured using LWD device for each test. The highest modulus and the lowest modulus were observed at test 5 and test 3, respectively, while either test section was not geogrid-stabilized sections. The average modulus value for stabilized test sections and non-stabilized sections were 24.3 MPa and 24.2 MPa, respectively. Therefore, it could be concluded that the LWD test results did not indicate the meaningful effect of the geogrid stabilization. This result could be attributed to the influence depth of the LWD test. The influence depth of LWD device was reported to be 0.5 to 1.8 times the loading plate diameter depending on testing conditions (Mooney & Miller, 2009; Senseney & Mooney, 2010). The thickness of the unbound aggregates above the geogrid was 1.19 times the loading plate diameter, which might be thicker than the influence range of the LWD device. Further, previous studies have reported no measurable benefits of geogrid-stabilization observed from LWD modulus measurements (Tang et al., 2013; Tingle & Jersey, 2009).

Table 5. Surface modulus results from LWD tests.

Test no.	Surface modulus (MPa)	Geogrid placement
2	26.2	GG2-stabilized
3	18.16	No geogrid
4	23.4	GG2-stabilized
5	27.34	No geogrid
6	23.28	GG2-stabilized
7	27.12	No geogrid

4 SUMMARY AND CONCLUSIONS

Quantification of local stiffness increases in geogrid-stabilized aggregate systems can provide important layer material characterization and analysis inputs in the development mechanistic-empirical design procedures for flexible pavements. A bender element (BE) field sensor was utilized to evaluate the local stiffness properties of unbound aggregates in the vicinity of an installed geogrid via shear wave velocity measurements. Dense-graded crushed stone aggregates were compacted in a large-scale laboratory testbed over a geofoam layer. Several shear wave velocity measurement tests were conducted with five levels of static surcharge loadings providing different confinement levels. Two geogrids were installed one at a time near the bottom of the aggregate layer during the construction and testing of geogrid-stabilized aggregate surfaced pavement sections, whereas the control sections were compacted without geogrid. The two punched and drawn geogrids evaluated in this study had different triangular aperture sizes. Shear wave velocities were measured using a BE field sensor installed at three different heights above the geogrid. In addition, dynamic cone penetrometer (DCP) and lightweight deflectometer (LWD) tests were performed on the constructed aggregate layers.

The shear wave velocities and the extents of the stiffened zone near two geogrids with different sized triangular apertures were successfully quantified using BE field sensors. The extents of the stiffened zone of the dense-graded aggregates generated by geogrid stabilization were between 15.2 cm (6 in.) and 25.4 cm (10 in.) above the geogrid. For this dense-graded aggregate material, GG2 geogrid with a smaller aperture size was more effective for geogrid stabilization, which is in accordance with the previous research findings from triaxial testing of BE pair instrumented aggregate specimens. In addition, DCP test results indicated that the geogrid-stabilized sections required a higher number of blow counts to penetrate down towards the geogrid location, and the GG2-stabilized section was stiffer than the GG1-stabilized section. However, the surface moduli from LWD tests were not of much use for measuring the effect of geogrid stabilization for unbound aggregates. In conclusion, BE field sensor successfully quantified the level and the extent of stiffening above the geogrid location to determine mechanically stabilized layer profiles which is quite critical regarding the

establishment of stiffness enhancement of geogrid-stabilized aggregates in the proximity of geogrid for mechanistic pavement analysis.

5 ACKNOWLEDGEMENTS

The research described in this paper was undertaken through US Army Corps of Engineers Contract W912HZ19P0047, entitled, "Development and Use of Bender Element and SmartRock Advanced Sensor Technologies for Field Instrumentation – ERDC SMART Runway Initiative (BAA 18-0104)." The research effort was partially supported by the GSI Fellowship of Geosynthetic Institute. The authors would like to thank Illinois Center for Transportation research engineers Greg Renshaw and Uthman Mohamed Ali for their help with laboratory tests.

6 REFERENCES

Barker, W.R. Open-Graded Bases for Airfield Pavements. Miscellaneous Paper GL-86. U.S. Army Corps of Engineers Waterways Experiment Station, Vicksburg. Miss., 1987.

Byun, Y.H. and Tutumluer, E. 2017. Bender Elements Successfully Quantified Stiffness Enhancement Provided by Geogrid–Aggregate Interlock. Transp. Res. Rec. 2656, 31–39.

Chen, C., McDowell, G.R., Thom, N.H., 2014. Investigating Geogrid-Reinforced Ballast: Experimental Pull-Out Tests and Discrete Element Modeling. Soils Found. 54 (1), 1–11.

Chen, Q., Hanandeh, S., Abu-Farsakh, M., and Mohammad, L. 2018. Performance evaluation of full-scale geosynthetic reinforced flexible pavement. Geosynthetics International, 25(1), 26-36.

Clayton, C.R.I., 2011. Stiffness at small strain: research and practice. Géotechnique. 61(1): 5-37.

Jewell, R.A., G. Milligan, R.W. Sarsby, and D. Dubois. 1984. Interaction between Soil and Geogrids. Polymer Grid Reinforcement. Proceedings of a Conference sponsored by the Science and Engineering Research Council and Netlon Ltd, London, 22-23.

Kang, M., Kim, J. H., Qamhia, I.I.A., Tutumluer, E., and Wayne, M.H, 2020. Geogrid Stabilization of Unbound Aggregates Evaluated Through Bender Element Shear Wave Measurement in Repeated Load Triaxial Testing. Transportation Research Record. 2674(3): 113-125.

Kang, M., Qamhia, I.I.A., Tutumluer, E., Hong, W.T., and Tingle, J.S., 2021. Bender Element Field Sensor for the Measurement of Pavement Base and Subbase Stiffness Characteristics. Transportation Research Record. doi: 10.1177/0361198121998350

Kinney, T.C., D.K. Stone, and J. Schuler, 1998. Using Geogrids for Base Reinforcement as Measured by Falling Weight Deflectometer in Full-Scale Laboratory Study. Transportation Research Record. 1611: 70–77.

Konietzky, H., te Kamp, L., Gröger, T., Jenner, C. 2004. Use of DEM to Model the Interlocking Effect of Geogrids under Static and Cyclic Loading. In: Shimizu, Y., Hart, R., Cundall, P. (Eds.), Numerical Modeling in Micromechanics via Particle Methods. A.A. Balkema, Rotterdam, 3–12.

Kwon, J. and Tutumluer, E. 2009. Geogrid Base Reinforcement with Aggregate Interlock and Modeling of Associated Stiffness Enhancement in Mechanistic Pavement Analysis. Transp. Res. Rec. 2116: 85–95.

Lee, J. S., and Santamarina, J. C., 2005. Bender Elements: Performance and Signal Interpretation. Journal of Geotechnical and Geoenvironmental Engineering. 131(9):1063–1070.

McDowell, G.R., Harireche, O., Konietzky, H., Brown, S.F., Thom, N.H. 2006. Discrete Element Modeling of Geogrid-Reinforced Aggregates. Proc. Inst. Civ. Eng. Geotech. Eng. 159 (1), 35–48.

Mooney, M.A. and Miller, P.K., 2009. Analysis of lightweight deflectometer test based on in situ stress and strain response. Journal of geotechnical and geoenvironmental engineering, 135(2): 199-208.

Moraci, N. and Recalcati, P. 2006. Factors Affecting the Pullout Behavior Of Extruded Geogrids Embedded in a Compacted Granular Soil. Geotextiles and Geomembranes, 24(4), 220-242.

NCHRP 1-37A Guide for Mechanistic–Empirical Design of New and Rehabilitated Pavement Structures. Final Report. NCHRP, ARA Inc., and ERES Consultants Division, Washington, D.C., March 2004

Norwood, G.J., 2019. Cyclic Plate Testing of Reinforced Airport Pavements-Phase I: Geogrid. Final Report No. DOT/FAA/TC-19/3, Federal Aviation Administration William J. Hughes Technical Center Aviation Research Division, Atlantic City International Airport, NJ.

Peng, X. and Zornberg, J.G. 2017. Evaluation of Load Transfer in Geogrids for Base Stabilization Using Transparent Soil. Procedia engineering, 189, 307-314.

Qian, Y., Tutumluer, E., Mishra, D., and Kazmee, H. 2015. Geogrid-Aggregate Interlocking Mechanism Investigated via Discrete Element Modeling. Geosynthetics 2015, February 15-18, 2015, Portland, Oregon.

Santamarina, J.C., Klein, K.A., and Fam, M.A., Soils and Waves - Particulate Materials Behavior, Characterization and Process Monitoring. Wiley, New York. 2001.

Senseney, C.T. and Mooney, M.A., 2010. Characterization of two-layer soil system using a lightweight deflectometer with radial sensors. Transportation Research Record, 2186(1): 21-28.

Siabil, S. G., Tafreshi, S. M., & Dawson, A. R., 2020. Response of pavement foundations incorporating both geocells and expanded polystyrene (EPS) geofoam. Geotextiles and Geomembranes, 48(1), 1-23.

Sugimoto, M. and Alagiyawanna, A.M.N. 2003. Pullout Behavior of Geogrid by Test and Numerical Analysis. Journal of Geotechnical and Geoenvironmental Engineering, 129(4), 361-371.

Tang, X., Stoffels, S.M., and Palomino, A.M., 2013. Resilient and Permanent Deformation Characteristics of Unbound Pavement Layers Modified by Geogrids. Transportation Research Record, 2369(1), 3–10.

Tingle, J. S., and Jersey, S. R., 2009. Full-scale evaluation of geosynthetic-reinforced aggregate roads. Transportation research record, 2116(1), 96-107.

Tutumluer, E, Huang, H., and Bian, X. 2009. Research on the Behavior of Geogrids in Stabilization Applications, In Proceedings of the Jubilee Symposium on Polymer Geogrid Reinforcement, September 8, 2009, London, UK.

US Environmental Protection Agency. 2020. The 2019 EPA Automotive Trends Report.

Webster, S. L., 1993. Geogrid reinforced base courses for flexible pavements for light aircraft: Test section construction, behavior under traffic, laboratory tests, and design criteria. Technical Report GL-93-6. U.S. Army Corps of Engineers Waterways Experiment Station, Vicksburg. Miss.

Xiao, Y., E. Tutumluer, Y. Qian, and J. Siekmeier, 2012. Gradation Effects Influencing Mechanical Properties of Aggregate Base and Granular Subbase Materials in Minnesota. Transportation Research Record: Journal of the Transportation Research Board, 2267:14-26.

Yoder, E. J. and Witczak, M. W. 1991. Principles of pavement design. John Wiley & Sons.

Zhou, J., Chen, J.F., Xue, J.F., Wang, J.Q. 2012. Micro-mechanism of the Interaction between Sand and Geogrid Transverse Ribs. Geosynthetics Int. 19 (6), 426–437.

Zou, Y., Leo, C. J., & Small, J. C. 2000. Behavior of EPS geofoam as flexible pavement subgrade material in model tests. Geosynthetics International, 7(1), 1-22.